IOP Publishing Semiconductor Science and Technology

Semicond. Sci. Technol. **38** (2023) 075002 (11pp) https://doi.org/10.1088/1361-6641/acd2fa

Role of graphene nanoparticles on the electrophysical processes in PVP and PVP:$ZnTiO_3$ polymer layers at Schottky diode (SD)

Ali Barkhordari[1,*], **Hamid Reza Mashayekhi**[1], **Pari Amiri**[2,7], **Şemsettin Altındal**[3] **and Yashar Azizian-Kalandaragh**[2,4,5,6,*]

[1] Faculty of Physics, Shahid Bahonar University of Kerman, Kerman, Iran
[2] Department of Engineering Sciences, Faculty of Advanced Technologies, Sabalan University of Advanced Technologies (SUAT), Namin, Iran
[3] Department of Physics, Faculty of Sciences, Gazi University, Ankara, Turkey
[4] Department of Photonics, Faculty of Applied Sciences, Gazi University, 06500 Ankara, Turkey
[5] Photonics Application and Research Center, Gazi University, 06500 Ankara, Turkey
[6] Department of Physics, University of Mohaghegh Ardabili, PO Box 179, Ardabil, Iran
[7] Department of Engineering Sciences, University of Mohaghegh Ardabili, Ardabil, Iran

E-mail: alibarkhordari20@yahoo.com and yashar.a.k@gmail.com

Received 13 December 2022, revised 14 April 2023
Accepted for publication 5 May 2023
Published 18 May 2023

Abstract

In this paper, a polyvinyl pyrrolidine (PVP) polymer layer is inserted between the metal–semiconductor (MS) structure to manufacture a metal–polymer–semiconductor (MPS) structure or Schottky diode (SD). The zinc titanate and graphene nanostructures were doped into the PVP layer individually and together to improve the electrical performance of the MPS-type SD. The crystalline size, surface morphology, and band gap energy of the $ZnTiO_3$ nanostructures are examined by the x-ray diffraction (XRD), field-emission scanning electron microscopy (FESEM), and ultraviolet–visible (UV–Vis) spectroscopy, respectively. It is common to measure the current–voltage (I–V) features (at ±3 V) of these five structures for calculating the reverse saturation current (I_0), barrier height, ideality factor (n), series (R_s), and shunt (R_{sh}) resistances as the main electrical parameters utilizing the thermionic emission, Norde, and Cheung models. Also, the forwarded-bias energy-dependent surface states density (N_{ss}) and the forward/reverse biased current conduction mechanisms are studied and discussed. The rectifying ratio (RR) of Al/PVP:Gr-$ZnTiO_3$/p-Si SD has the highest increase among these five SDs while the lowest I_0 and highest R_{sh} are related to the Al/PVP:Gr/p-Si (MPS2) and Al/PVP:$ZnTiO_3$/p-Si (MPS3) SDs, respectively. Therefore, doping Gr into the PVP interlayer increases the electrical conduction in the SDs although PVP:Gr-$ZnTiO_3$ polymer layer improves the RR of SDs.

Keywords: polyvinylpyrrolidone (PVP), graphene (Gr), zinc titanate ($ZnTiO_3$), Schottky diodes (SDs), electric properties, conduction mechanism

(Some figures may appear in colour only in the online journal)

---

[*] Authors to whom any correspondence should be addressed.

1361-6641/23/075002+11$33.00 Printed in the UK

1. Introduction

In solid-state physics, the metal–semiconductor (MS)-type Schottky diode (SD) with/without a thin insulator or polymer interlayer is potentially exciting and can be used either for rectifying or non-rectifying processes [1–3]. At higher the thermal energy, a sufficiently great potential barrier height (BH) permits the electronic current to flow just in one path called a rectifying MS structure, whereas lower BHs form an ohmic MS junction because of the non-depleting semiconductors. Moreover, the operational SDs are vital in all semiconductor instruments like the MS-type SD with and without a polymer interlayer (MS, MIS), transistors, and solar cells. Despite the conventional insulators created by old-fashioned procedures, the main scientific and technological obstacle for the MS-type SD is to expand their performances and decrease their costs by employing different useful interfacial layers like metal-doped polymer interlayer, metal-oxide dopants, and materials with high dielectric properties [4–8]. Furthermore, the developed common insulator layer (e.g. SiO_2 or SnO_2) between metal and semiconductor with the conventional techniques are not able to passivate dangling bonds activated at the surface of semiconductor and decline the leakage current [1, 3–5, 9, 10].

With the utilization of an interfacial organic/polymer layer in pure or doped form, the optic, electric, and dielectric improvements of these instruments have attracted much attention owing to several reasons such as weightless, suitable mechanical stability, large surface space relative to volume rate, good flexibility, high capacity in charge/energy-storage, large dielectric stability, and simple procedure methods [5, 11, 12]. Therefore, controlling and manipulating the BH of SD to raise its performance is intriguing. The value of ideality factor (n) should be unity in ideal case ($n = 1$), but it is usually deviated from the ideal case ($n > 1$) due to the existence a native or deposited interfacial layer such as an insulator/oxide, polymer, and ferro-electric materials between metal and semiconductor, its thickness (d_i) and dielectric (ε_i) values, density of surface states (N_{ss}) between the interfacial layer and semiconductor interface, and the thickness of depletion layer width ($W_d = (2\varepsilon_s\varepsilon_o V_i/qN_a)^{0.5}$) depend on the doping level of donor or acceptor atoms (N_d or N_a) into pure semiconductor as given [$n = 1 + d_i/\varepsilon_i\ (\varepsilon_i/W_d + qN_{ss})$]. In addition, the values of n along with the mechanisms of current conduction in the metal–polymer–semiconductor (MPS)-type SD are affected by different processes including the electrons tunneling in the potential barrier with surface states, generation and recombination (GR) of electron–hole pairs, and barrier lowering due to the image-force [1–3, 5, 8–10].

It is useful to note that the polymer molecules are chemically long-chain. Thin films produced by synthesizing the polymers have gained attraction due to several advantages including large stability, inexpensiveness, simple processing and growth [13]. As a result of these benefits, polymers are becoming increasingly popular in the fabrication of electronic devices. Despite this, the use of polymers may reduce the electrical conductivity. Doping metal/metal-oxide atoms in these polymers can enhance their electrical conductivity [14]. How to build the Ni/SiO_2/p-Si/Al SD and temperature effects on dielectric features of the SD by measuring the C–V–f and G–V–f (in ranges of 95–300 K and 10 kHz–1 MHz for the temperature and frequency) were reported by Kumar and Chand [15]. As a result, the structure's permittivity was increased with increasing temperature and decreased with increasing frequency. Moreover, both Au/n-Si and Au/(%7Graphene-PVA)/n-Si-type SDs with various graphene contents were built by Al-Dharob *et al* [5], and it was observed that the best doping ratio of graphene into the PVA polymer layer for optimum values of electronic parameters in MPS is 7% compared to the MS-type SD. Rajagopal Reddy *et al* [16] measured the C–V and I–V characteristics of the Au/$Bi_{0.5}Na_{0.5}TiO_3$-$BaTiO_3$(BT)/n-GaN SD at the temperature range from 120 K to 420 K and discovered that the BH and N_{ss} in the considered MPS diode increase with increasing the temperature.

Two wideband semiconductors with special effects and extensive applications, i.e. TiO_2 and ZnO, are very interesting in either single materials or ZnO-TiO_2 composites [17–19]. For instance, unique properties and versatile applications in transparent electronics, chemical sensors, piezoelectric devices, spin electronics, and UV light emitters are several advantages of ZnO which are studied in the literature [20–23]. ZnO has a significant exciton binding energy (60 meV) compared to other materials commonly used as semiconductors for blue-green light-emitting instruments, such as ZnSe (22 meV) and GaN (25 meV) [24]. TiO_2 is, however, a semiconductor being non-toxic, stable in an aqueous solution, and somewhat inexpensive. In addition, the exceptional photocatalytic property of TiO_2 has been caused by its wide band gap and long lifetime of photo-generated holes and electrons [25]. However, TiO_2 has significant drawbacks during the photocatalytic process:

(i) The less use of solar spectrum, and
(ii) a relatively high electron–hole recombination rate.

ZnO doping can solve these issues and improve the activity of TiO_2 photocatalysts [26]. A perovskite-type oxide structure, i.e. $ZnTiO_3$, could be considered a kind of microwave resonator [27], gas sensor [28] (for ethanol, NO, CO, and so on), microelectronics [29], metal-air barriers [30], and high-performance catalysts [31] for the total oxidation of hydrocarbons or CO and NO reduction [32], and paint pigment [33]. The ZnO–TiO_2 system contains several compounds, including α-Zn_2TiO_4 (cubic), zinc titanate ($ZnTiO_3$, cubic and hexagonal), and $Zn_2Ti_3O_8$ (cubic) [34, 35]. Since the compound decomposes into α-Zn_2TiO_4 and rutile TiO_2 at about 945 °C, the preparation of pure $ZnTiO_3$ from a mixture of ZnO and TiO_2 with 1:1 has not been successfully done. Some ways exist to prepare $ZnTiO_3$ powder, including solid state reactions [36] and sol–gel [37].

Graphene is a two-dimensional structure composed of a single layer of hexagonal carbon and it has extraordinary such as high density and mobility, optical conductivity, and mechanical properties [38]. Therefore, it has been considered a very suitable candidate for replacing Si in the photonic and electronic instruments [39]. When single layer of graphene is placed on top of each other, they form a three-dimensional bulk of graphite, and the van der Waals force bonds the plates and the distance among them is about 0.335 nm [39]. Polyvinyl pyrrolidine (PVP) is also an excellent polymer used to fabricate the MPS-type SD and it being constructed quickly and inexpensively, having suitable conductivity, high stability, and having no toxic effects [40].

In this work, five SDs with the structures of Al/p-Si (MS), Al/PVP/p-Si (MPS1), Al/PVP:Gr/p-Si (MPS2), Al/PVP:$ZnTiO_3$/p-Si (MPS3), and Al/PVP:Gr-$ZnTiO_3$/p-Si (MPS4) were fabricated to examine the impact of these interfacial layers on the principal electric parameters of the MS-type SD. To this end, the material preparation and fabrication processes of theses SDs is briefly explained. Next, the XRD pattern, FESEM image, and UV–Vis spectrum are used to estimate the crystalline size, surface morphology, and band gap energy of the $ZnTiO_3$ nanostructures, respectively. Then, the I–V characteristics of the SDs are measured and three techniques, i.e. thermionic emission (TE), Norde, and Cheung, are applied for calculating and comparing the basic electric parameters of these five diodes, such as n, BH, I_0, R_{sh} and R_s. The N_{ss} profile in terms of energy and the current transport/conduction processes at forward and reverse bias voltage will be studied. Finally, the effect of the different interlayers on the performance of the MPS-type SD compared to the MS SD and the physical mechanisms occurring in them are discussed in detail.

2. Experimental details

$TiCl_4$ (⩾99%) and $Zn(CH_3COO)_2{\cdot}2H_2O$ (⩾99%) were bought from ROYALEX and Merck Companies, respectively. Our recently published paper [41], has reported the preparation of TiO_2 nano-powders. To synthesize the $ZnTiO_3$ nanostructures, we initially prepared 20^{cc} of $Zn(CH_3CO_2)_2$ (0.2 M), 20^{cc} of NaOH (0.2 M), and 20^{cc} of TiO_2 (0.15 M) solutions in separate beakers. In order to provide TiO_2 nanostructures, 22^{cc} of $TiCl_4$ in liquid phase has been added dropwise to 20^{cc} of NaOH (0.2 M) on a magnetic stirrer and after measuring the pH of the mixture, it was irradiated by microwaves of 800 W for 10 min. The obtained white mixture was rinsed by deionized water and dried at room temperature. Then the TiO_2 and NaOH solutions were added drop by drop to the $Zn(CH_3CO_2)_2$ solution at room temperature under an ultrasonic irradiation. The result was then placed in a microwave instrument and exposed to microwave radiation at 800 W for 10 min. Then the product was washed during centrifugation and dried at room temperature. Finally, the obtained nanopowder was annealed at 700 °C for two hours. Figure 1 shows schematically the preparation process and fabrication of the SDs in this work.

It should be noted that a p-type Si wafer with the thickness of 300 μm was applied in this work. A 100 nm thickness high pure (99.999%) aluminum (Al) layer was thermally evaporated on the whole backside of p-Si wafer at 10^{-6} Torr and then annealed at 500 °C temperature to perform a low resistivity or good ohmic contact. Moreover, a PVP polymer layer with/without dopant with a thickness of 100 nm was deposited on the top surface of the Si wafer using a spin coater system. At last, 100 nm masks were coated on the PVP polymer layer with/without dopant as ohmic contacts in tablet shape.

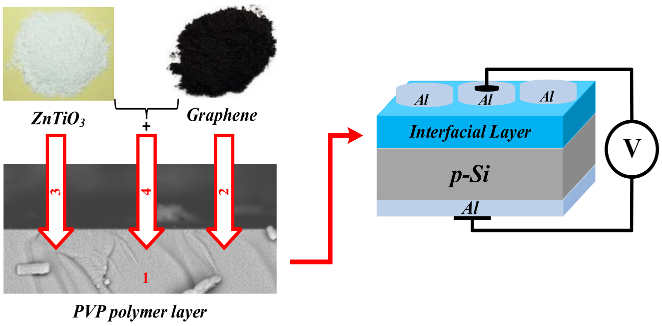

Figure 1. Schematic of the preparation process and fabrication of SDs.

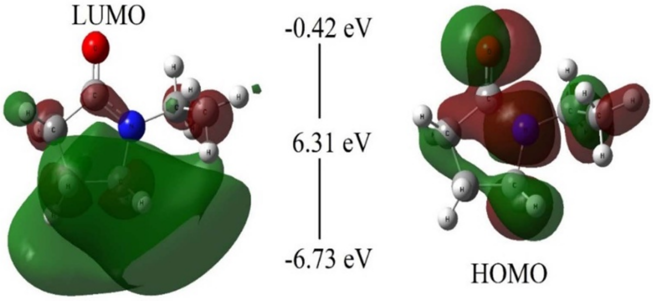

Figure 2. HOMO and LUMO contour maps of PVP molecule.

The highest occupied molecular orbital (HOMO), lowest unoccupied molecular orbital (LUMO) energies and energy gap between them for the PVP polymer were also calculated (see figure 2). This gap is an important indicator for the detection of the molecular electrical transport. In addition, the energy of HOMO refers to the ionization potential and the energy of LUMO refers to the electron affinity [42]. The calculated energies of PVP are −0.42 eV for LUMO and −6.73 eV for LUMO. The energy gap is determined as 6.31 eV. Moreover, the HOMO and LUMO contour maps of PVP molecule in vacuum were presented in figure 2. The negative parts of the molecule are represented in red and the positive parts are represented in green.

3. Results and discussion

3.1. XRD analysis of $ZnTiO_3$

The XRD pattern of $ZnTiO_3$ nanostructures synthesized by the microwave assisted-method is depicted in figure 3. The peaks presented in this pattern are related to the $ZnTiO_3$ and TiO_2 materials whose structures correspond to the tetragonal and

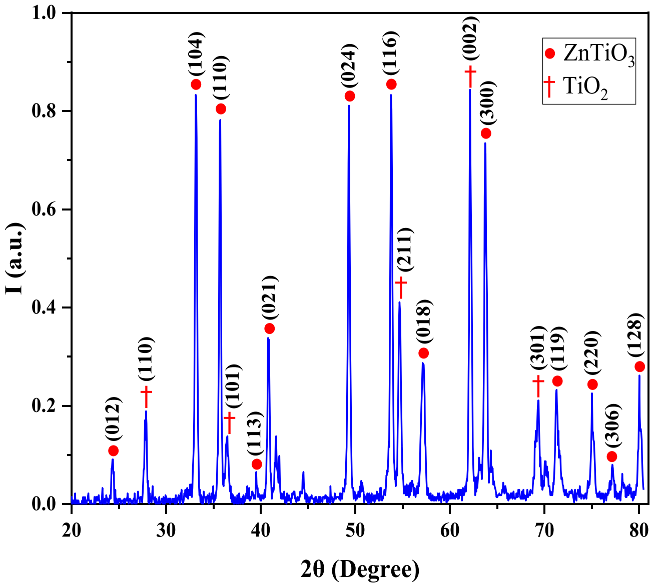

Figure 3. XRD pattern of $ZnTiO_3$ nanostructures.

rhombohedral with lattice constant of $a = 5.08$ Å, $c = 13.9$ Å and $a = 4.59$ Å, $c = 2.95$ Å, respectively. Furthermore, the crystalline planes of $ZnTiO_3$ nanostructures represented in the XRD pattern (012), (104), (110), (113), (021), (024), (116), (018), (300), (119), (220), (306) and (128) are corresponding to the angles 2θ of 24.3°, 33.1°, 35.7°, 39.5°, 40.7°, 49.3°, 57.1°, 63.7°, 71.3°, 75.0°, 77.2°, and 80.0°, respectively. In order to calculate the average crystalline size of $ZnTiO_3$ nanostructures, the Debye-Scherrer equation must be used which is given by [5]:

$$D = k\lambda/\beta\cos\theta \tag{1}$$

with k being the Scherer constant (∼0.9), λ the x-ray wavelength (=15.4056 nm), β the full width at half the maximum of the XRD peak and θ the Bragg angle [5]. The zinc titanate nanostructure's average crystalline size is 29 nm.

3.2. SEM image

Recorded images of the FESEM microscope might be used to study the morphology of the zinc titanate nanostructures. The surface-morphology patterns of the synthesized zinc titanate nanostructures are illustrated in figure 4. Since the sizes of real particles are hard to see, the structure of polydispersity nanoparticles can be seen in different configurations with an average size of <50 nm. All nanoparticles have agglomerated with each other's and made clusters in micron-size.

Figure 4. SEM image of the $ZnTiO_3$ nanostructures with magnification of 500k×.

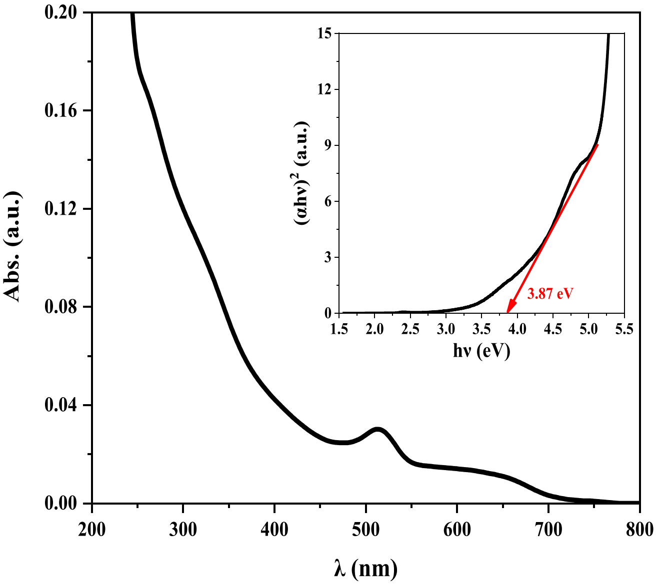

Figure 5. UV–Vis absorption spectra and the band gap energy profile of the $ZnTiO_3$ nanostructures.

3.3. UV–Vis spectroscopy

Figure 5 presents the UV–Vis absorption spectrum in the wavelength range from 200 nm to 800 nm and the band gap energy profile of $ZnTiO_3$ nanostructures using Tauc's equation. This equation gives the optical band gap by [16]:

$$\alpha h\upsilon = C(h\upsilon - E_g)^m \tag{2}$$

with α being the absorption-coefficient, $h\nu$ the emitted photon energy, C an arbitrary constant and E_g band gap energy [16]. The parameter m could have a value of 0.5 for direct and 2 for indirect transitions. For condition $(\alpha h\upsilon)^2 = 0$, the intercept point is equal to the quantity E_g, because the linear part is extrapolated to the $h\nu$ axis. As a result, the band gap energy value was also computed as 3.87 eV.

3.4. TE method

The I–V characteristic curves of the prepared structures are logarithmically represented in figure 6 at forward and reverse bias voltages. These profiles show that the rectifying behavior (rectifying ratio (RR) $= I_{\text{forward}}/I_{\text{reverse}}$ at ±3 V) of these diodes

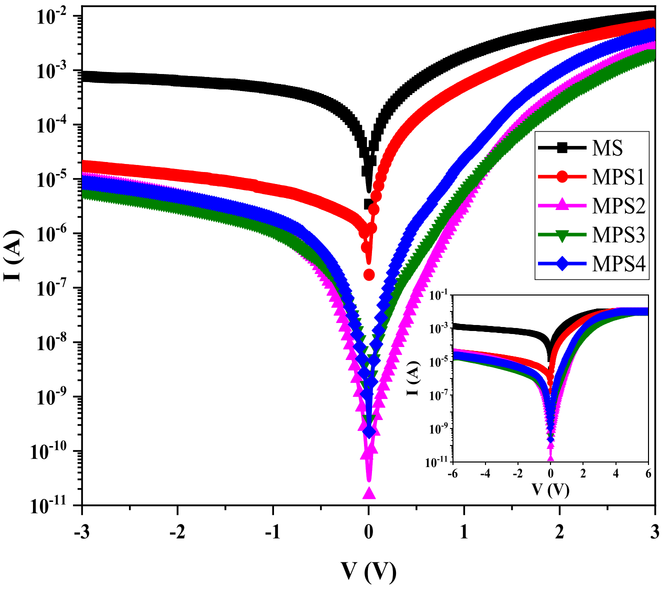

Figure 6. The I–V curves of the prepared five different SDs.

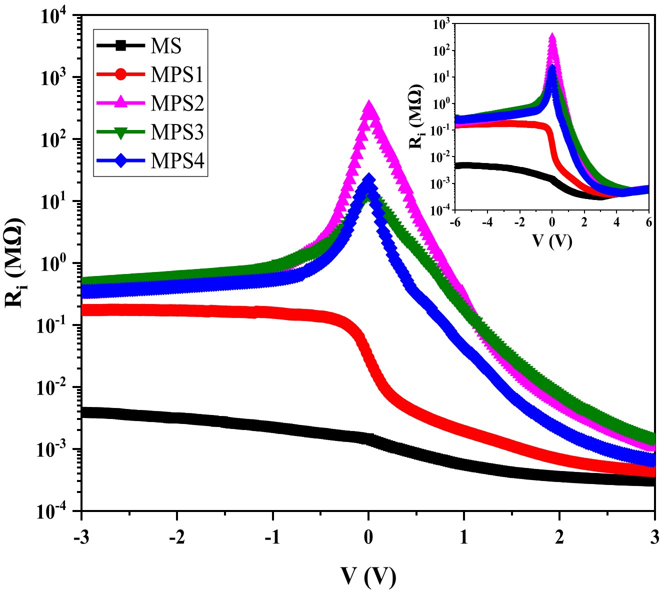

Figure 7. The R_i–V profiles of the prepared five different SDs.

is reasonable. The TE scheme can be applied to examine the I–V features of the prepared MS- and MPS-type SDs.

The relation between the current and voltage in a SD for $V \geqslant 3kT/q$ and with the consideration of an R_s at the forward bias voltage is given by [37, 38]

$$I = I_0 \left[\exp\left(\frac{q(V - IR_s)}{nkT}\right) - 1\right]. \tag{3}$$

The linear region of ln(I)–V curve at zero voltage could be used to calculate the quantity I_0 as [38]:

$$I_0 = AA^* T^2 \exp\left(-\frac{q\varphi_{B0}}{kT}\right). \tag{4}$$

The parameter A refers to contact space, A^* denotes the Richardson constant, and φ_{B0} is zero-bias BH. The values of I_0 for MS-, MPS1-, MPS2-, MPS3-, and MPS4-type SDs is equal to 6.13×10^{-5} A, 5.03×10^{-6} A, 2.78×10^{-10} A, 6.19×10^{-9} A, and 7.56×10^{-9} A, respectively. In addition, the BH value at $V = 0$ could then be expressed by [39]:

$$\varphi_{B0} = \frac{kT}{q} \ln\left(\frac{AA^* T^2}{I_0}\right). \tag{5}$$

The BHs of MS-, MPS1-, MPS2-, MPS3-, and MPS4-type SDs are 0.596 eV, 0.661 eV, 0.914 eV, 0.834 eV, and 0.829 eV, respectively. The value of n is calculated using the slope value in the following [39, 40]:

$$n = \frac{q}{kT}\left(\frac{dV}{d(\ln I)}\right). \tag{6}$$

The value of n for these diodes is 7.73 for MS, 5.29 for MPS1, 3.33 for MPS2, 4.49 for MPS3, and 3.30 for MPS4. The value of RR for MPS4 (~541) diode is higher than that of the other diodes at ±3 V (see table 1). Also, the leakage current of the MPS2 structure is almost five orders of magnitude smaller than the MS one. Using the PVP:Gr-ZnTiO$_3$ interlayer, the n shows the maximum reduction. To significantly reduce the leakage current while decreasing n, pure graphene should be doped in the PVP polymer interfacial layer sandwiched between the metal and semiconductor.

It should be noted that several different sources lead to the R_s and they can be listed as the ohmic and rectifier or Schottky contact created on the semiconductor layer, dust and dirt remaining between the contacts in the cleaning step of manufacture procedures, semiconductor bulk resistance, and the largely inhomogeneous distribution of dopant atoms at the semiconductor layer [1, 40–44]. Besides, the R_{sh} might be formed by the leakage of oxide/current ways across the interlayer, patches from the probe wire to the ground, and some imperfections in the contact area [45–49]. When diode has an interfacial layer, by considering R_s ($V_{Rs} = I{\cdot}R_s$) and N_{ss}, the applied positive bias voltage (V_a) would share among them and depletion layer with the relation of $V_a = V_i + V_{Rs} + V_d + V_{ss}$. As a result, the profile of ln$I$–V would deviate from the linearity at enough high forward biases especially due to the R_s and interfacial layer.

As known, the resistance ($R_i = dV_i/dI_i$) of the diode for any bias voltage can be calculated from the basic Ohm's Law by using the current–voltage (I–V) data. But, the real values of R_s and R_{sh} are corresponding to enough high forward and reverse bias voltages. As can be clearly seen in the figure 7, the value of R_i becomes as almost constant at about ±3 V. Thus, the real value of R_{sh} at −3 V was found as 3.89 kΩ for MS, 173 kΩ for MPS1, 310 kΩ for MPS2, 498 kΩ for MPS3, and 346 kΩ for MPS4, respectively. On the other hand, the real value of R_s at 3 V was found as 0.30 kΩ for MS, =0.43 kΩ for MPS1, 1.04 kΩ for MPS2, 1.44 kΩ for MPS3, and 0.64 kΩ for MPS4, respectively. These values indicate that the shunt resistances of MPS diodes are drastically increased compared to the MS diode thus the RR is enhanced which is most distinctive feature of these diodes. It means the ratio of the current at enough high

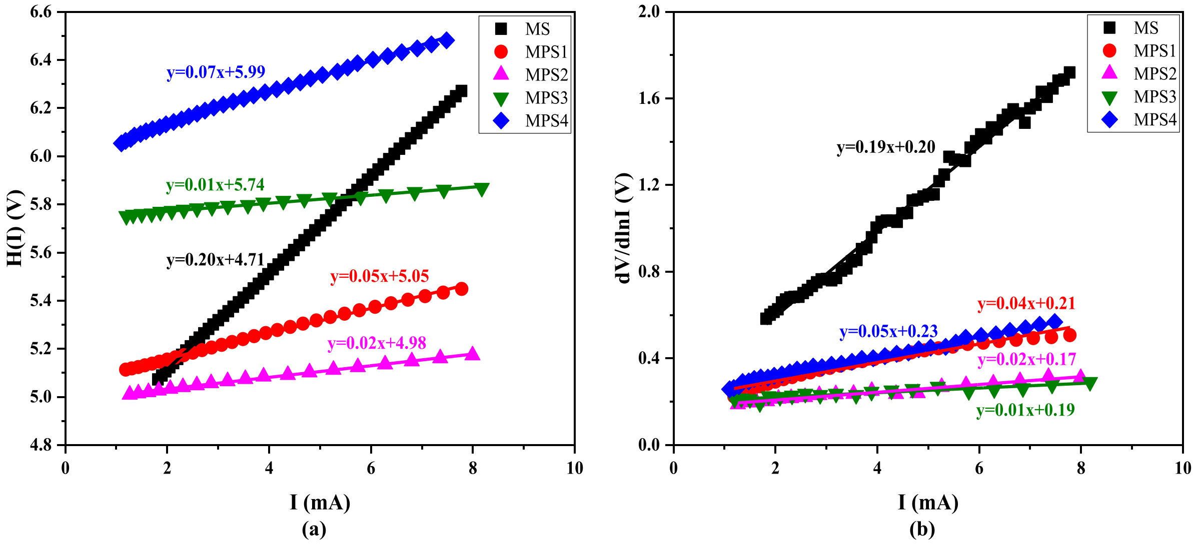

Figure 8. (a) $H(I)$ and (b) $\mathrm{d}V/\mathrm{dln}(I)$ versus I profiles of the prepared five different SDs.

forward bias voltage to the current at the same reverse bias voltage. However, the series resistances of the MPS-type SDs are slightly increased in relation to the MS-type SD.

3.5. Cheung method

Based on the Cheung functions, the R_s, n, and φ_B could be acquired by measuring the linear deviation of ln(I)–V profiles as follows [31]:

$$\frac{\mathrm{d}V}{\mathrm{d}\left(\ln I\right)} = IR_\mathrm{s} + \left(\frac{nkT}{q}\right) \tag{7a}$$

$$H\left(I\right) = V - \frac{nkT}{q}\ln\left(\frac{I}{AA^{*}T^{2}}\right) = IR_\mathrm{s} + n\varphi_\mathrm{B}. \tag{7b}$$

In figures 8(a) and (b), the functions $H(I)$ and $\mathrm{d}V/\mathrm{d}(\ln I)$ were depicted versus the electrical current for prepared SDs. The quantities n, R_s, and φ_B are calculated using the slopes of $\mathrm{d}V/\mathrm{d}(\ln I)$ and intercepts of $H(I)$, respectively.

3.6. Norde method

Another way for calculation of the values of the BH and R_s is using Norde function, $F(V)$, written as [41]:

$$F\left(V\right) = \frac{V}{\gamma} - \frac{kT}{q}\left[\ln\left(\frac{I\left(V\right)}{AA^{*}T^{2}}\right)\right] \tag{8}$$

here γ denotes an integer and must be greater than the value of n. The treatment of $F(V)$ versus V for five SDs using equation (8) is shown in figure 9. The concave point of $F(V)$ for the prepared SDs is appeared in different voltages.

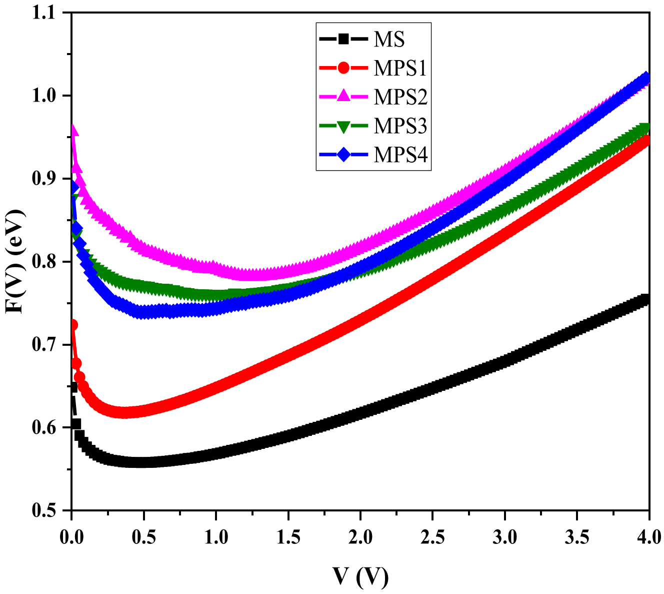

Figure 9. Changes of $F(V)$ vs the voltage of prepared five different SDs.

Through the corresponding values at the minimum in figure 9, the values of φ_B and R_s are obtained by using the following equations [41]:

$$\varphi_\mathrm{B} = F\left(V_\mathrm{min}\right) + \frac{V_\mathrm{min}}{\gamma} - \frac{kT}{q} \tag{9a}$$

$$R_\mathrm{s} = \frac{kT\left(\gamma - n\right)}{qI_\mathrm{min}}. \tag{9b}$$

V_min and I_min refer to the voltage and current at the extremum point of the $F(V)$ function. The values of φ_B and R_s for the prepared structures computed with the TE method,

Table 1. Electrical parameters of the prepared five different SDs obtained by various techniques.

Diode	I_0 (nA)	Φ_{B0} (eV) TE	Φ_{B0} (eV) Norde	Φ_{B0} (eV) $H(I)$	RR	R_s (kΩ) TE	R_s (kΩ) Norde	R_s (kΩ) $H(I)$	R_s (kΩ) dV/dln(I)	R_{sh} (kΩ)	n TE	n dV/dln(I)	$N_{ss} \times 10^{13}$ (eV^{-1} cm^{-2})
MS	6128	0.59	0.58	0.58	13	0.30	0.29	0.20	0.19	3.89	7.73	8.00	6.86
MPS1	5030	0.66	0.67	0.65	401	0.43	0.47	0.05	0.04	173	5.29	7.69	4.76
MPS2	0.27	0.91	0.93	0.87	298	1.04	4.54	0.02	0.02	310	3.33	5.77	0.15
MPS3	6.19	0.83	0.89	0.82	347	1.44	6.08	0.01	0.01	498	4.49	6.92	1.45
MPS4	7.56	0.83	0.87	0.80	541	0.64	2.67	0.07	0.05	346	3.30	7.54	0.42

Norde, and Cheung's functions are listed in table 1. The n value is reduced significantly when Gr-ZnTiO$_3$ is doped in the PVP polymer interfacial layer, whereas the BH of MS increases significantly when pure graphene is doped in the PVP polymer layer. In addition, along with the increase in φ_B and decrease in N_{ss} and n, the RR of the MPS diodes is larger than that of the MS one (the highest value of RR is related to the MPS4 structure among these diodes); hence, the MS structure's performance is enhanced by using the PVP, PVP:Gr, PVP:ZnTiO$_3$, and PVP:Gr-ZnTiO$_3$ polymer interlayers. It is seen that the values obtained by the various approaches agree with each other.

As can be observed, the leakage current (I_R) value of MPS3-type SD at the bias voltage of -3 V is nearly two orders of magnitude smaller than that of MS one (see figure 6), and the I_0 value at the bias voltage of 0 V for the MPS2-type SD is about 1000 times smaller than that of the MS one (see table 1). According to table 1, the higher amount of R_{sh} related to the MPS-type SDs, in comparison with this amount for the MS one, is a result of a decline in N_{ss} because of the presence of the large-dielectric interlayers and its passivated effect. For smaller amounts of I_0, n, and N_{ss}, and larger amounts of RR, R_{sh}, and BH, all these results show that the PVP interlayer with different doping, i.e. pure graphene, ZnTiO$_3$, Gr-ZnTiO$_3$, at the metal/semiconductor interface, rather than the typical SiO$_2$, results in optimized MS-type SD performance.

3.7. Energy-dependent interface states

The non-uniform distribution of doped atoms, combined with the interface states, results in less than the ideal behavior in a diode. The energy dependent profile of N_{ss} can be obtained from the forward bias I–V data by taken into account the voltage dependent value of ideality factor and BH by using Card and Rhoderick model [3]. In other words, Card and Rhoderick have devolved a general-representation for the N_{ss} as [3];

$$N_{ss}(V) = \frac{1}{q}\left[\frac{\varepsilon_i}{\delta}(n(V) - 1) - \frac{\varepsilon_s}{W_D}\right] \tag{10}$$

where W_D is the width of the depletion layer. The interfacial layer thickness (δ) was measured via a cross-section SEM image which is equal to 100 nm. Furthermore, an estimation of this quantity can be given by the interfacial layer capacitance ($C_i = \varepsilon_i \varepsilon_s A/d_i$), in which A is the rectifier contact area ($=7.85 \times 10^{-3}$ cm^2), ε_i and ε_s are also the permittivity of interlayer and semiconductor, respectively. For a p-type semiconductor, the energy difference between the valance band and the N_{ss} level could be described as [1–3, 33]:

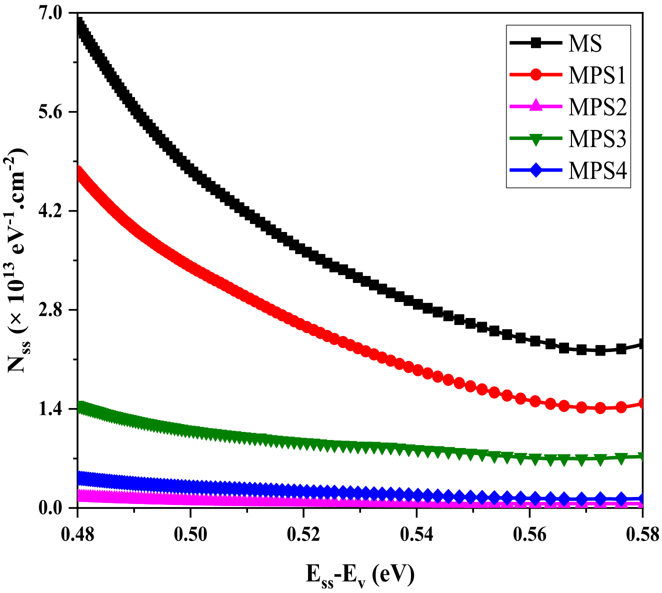

Figure 10. The energy-dependent profiles of N_{ss} for the prepared five different SDs.

$$E_{ss} - E_v = q(\varphi_e - V). \tag{11}$$

Using the relations of φ_e, $n(V)$, and R_s the is given by [33]:

$$\varphi_e - \varphi_{B0} = \left(1 - \frac{1}{n(V)}\right)V. \tag{12}$$

Using the equations (10)–(12), the profiles of N_{ss} in terms of energy can be plotted as figure 10.

Since the existence of the polymer interlayer results in semiconductor surface passivation [35, 36], the minimum value of N_{ss} among the prepared diodes is for the MPS2 ($\sim$0.15 × 10^{13} eV^{-1} cm^{-2}). It needs to be noted that N_{ss} of the MS-type SD ($\sim$6.86 × 10^{13} eV^{-1} cm^{-2}) is approximately reduced 46 times. To show this reduction in N_{ss}, the schematic diagrams of the energy-band of the MS- and MPS3-type SDs are demonstrated in figures 11(a) and (b), respectively. As

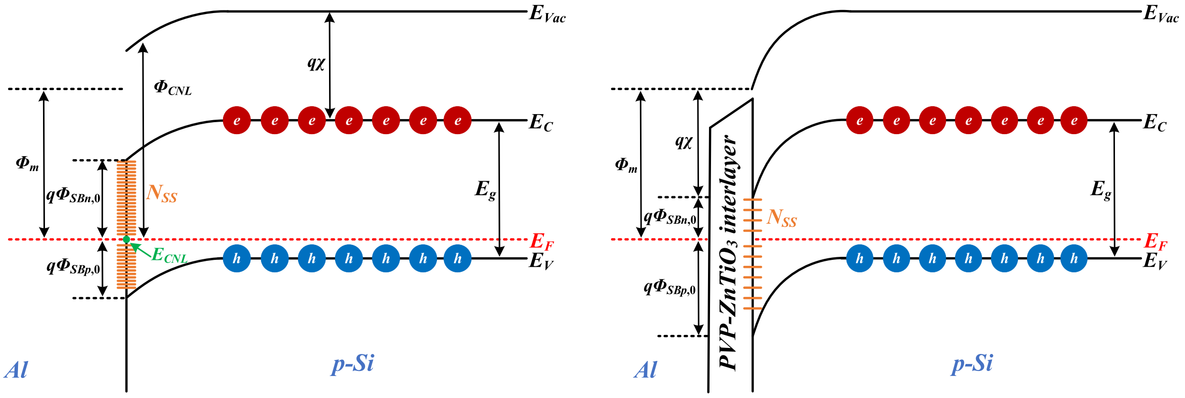

(a) (b)

Figure 11. Energy-band diagram of (a) MS and (b) MPS3 structures.

shown in figure 11, both in MS- and MPS-type SDs, the formation of BH and native or deposited an interfacial layer between metal and semiconductor, their homogeneity, and N_{ss} can be changed the conduction mechanisms (CMs) in these diodes [3, 9, 10]. N_{ss} or interface-traps (D_{it}) at M/S interface with an interfacial layer of high-defects density are assumed to be the primary cause for Fermi-level pinning. These surface-states in the bandgap of semiconductor known as meta-induced gap states (MIGS) can lead to Fermi level pining. These MIGS act as acceptors close to the valence band (E_{v}), while they are acting as donors at near the conduction band (E_{c}) of semiconductor and they can capture or release some electrons. Therefore, they can be donor/acceptor-like charges.

Fermi level pinning depend on metal work function (Φ_{m}) and the pinning factor S can be obtained as $S = \partial\Phi_{\mathrm{SB}}/\partial\Phi_{\mathrm{m}}$. In other words, Φ_{m} can change the Schottky barrier-height (Φ_{SB}) at M/S interface and a typical S has $0 \leqslant S \leqslant 1$ values. The thickness of interfacial layer is also very effective on the CMs and when its thickness is lower than at about 3 nm, these states/traps are in equilibrium with metal, while its thickness is higher a few nm they are in equilibrium with semiconductor [1–3, 9, 10].

3.8. Current conduction mechanisms (CCMs)/current transport mechanisms

Figure 12 depicts the ln(I_F) profiles as a function of V_F for the prepared diodes, including two regions for MS- and MPS1-type SDs and three regions for MPS2-, MPS3-, and MPS4-type SDs because of different mechanisms in the current conduction. These mechanisms investigate the impact of polymer interfacial layer on the electric current made by the unbound carriers. The deep traps formed in the interface are able to improve the charge transport that affect the current–voltage measurements. The ln(I_F) profiles in terms of the potential at forward bias have three different regions with various slopes which has been presented in figure 12(a) for the prepared structures. Different regions show different behaviors: at region (I) with a slope near unity, there is an ohmic behavior, i.e. I–V. The bias voltage is small in this region; therefore, the lower charges will be inserted in the semiconductor from electrodes [1, 33, 37]. The slope is greater than two in the region (II), and the electrical current changes exponentially, i.e. I–exp(V). In this region, the dominant CCM is recombination tunneling [18]. At the region (III), the behavior of electric current seems to be a power form, i.e. I–V^2. This is because the distribution of traps follows a transport mechanism of the space-charge limited current (SCLC) into the band gap of Gr, ZnTiO$_3$, and Gr-ZnTiO$_3$ nanostructures. The SCLC process occurs when the charge value in comparison with the injected charge value can be omitted at equilibrium condition. It must be noted that the trap filling up and the space-charge in the SCLC process result from the enhancement of the injected electrons from the electrodes [1, 33, 38].

The quantity ln(I_R) in terms of $V_R^{1/2}$ is shown in figure 12(b). The Poole-Frenkel emission (PFE) or Schottky emission (SE) mechanisms should be considered when studying CCMs in prepared diodes at reverse bias voltage. To overcome of the PFE process, the I_R can be described as [18, 33, 39]:

$$I_R = I_0 \exp\left(\frac{\beta_{\mathrm{PF}} V^{1/2}}{kTd^{1/2}}\right). \tag{13}$$

Conversely, the I_R is defined with the following relation provided that the SE process overcomes, i.e. we have [33]

$$I_R = AA^* T^2 \exp\left(-\frac{\varphi_{\mathrm{B}}}{kT}\right) \exp\left(\frac{\beta_{\mathrm{SC}} V^{1/2}}{kTd^{1/2}}\right) \tag{14}$$

here the β_{PF} is the coefficient of field-lowering for PFE mechanism and β_{SC} being this coefficient for SE mechanism. By this definition, the value of β_{PF} is two times greater than the β_{SC} amount, which is written as [1, 39]:

$$2\beta_{\mathrm{SC}} = \beta_{\mathrm{PF}} = \left(\frac{q^3}{\pi\,\varepsilon_0 \varepsilon_{\mathrm{r}}}\right)^{1/2}. \tag{15}$$

Parameter ε_{r} is the permittivity of the interlayer. Linear curves depicted in figure 12(b) show the experimental behaviors of ln(I_R) in terms of $V^{1/2}$ for considered diodes. The slopes of these lines known as the field lowering coefficient are equal to values of 1.81 × 10^{-6} eV^{-1} m$^{1/2}$ V$^{1/2}$

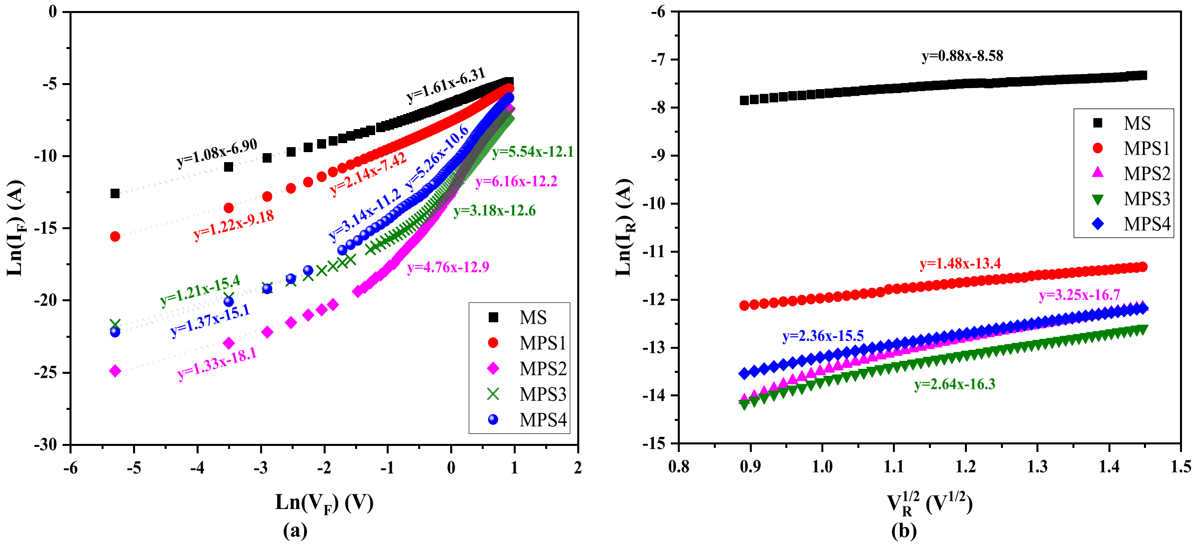

Figure 12. (a) The $\ln(I_F)$–V_F and (b) $\ln(I_R)$–${V_R}^{1/2}$ plots of the prepared five diodes.

for MS, 1.23×10^{-5} eV^{-1} m$^{1/2}$ V$^{1/2}$ for MPS1, 2.67×10^{-5} eV^{-1} m$^{1/2}$ V$^{1/2}$ for MPS2, 2.17×10^{-5} eV^{-1} m$^{1/2}$ V$^{1/2}$ for MPS3, and 1.98×10^{-5} eV^{-1} m$^{1/2}$ V$^{1/2}$ for MPS4 SDs. On the other hand, the theoretical amounts of $\beta_{\mathrm{PF}}(\mathrm{MS}) = 3.83 \times 10^{-5}$ eV^{-1} m$^{1/2}$ V$^{1/2,}$ $\beta_{\mathrm{PF}}(\mathrm{MPS1}) = 9.36 \times 10^{-6}$ eV^{-1} m$^{1/2}$ V$^{1/2}$, $\beta_{\mathrm{PF}}(\mathrm{MPS2}) = 3.22 \times 10^{-5}$ eV^{-1} m$^{1/2}$ V$^{1/2}$, $\beta_{\mathrm{PF}}(\mathrm{MPS3}) = 1.25 \times 10^{-5}$ eV^{-1} m$^{1/2}$ V$^{1/2,}$ and $\beta_{\mathrm{PF}}(\mathrm{MPS4}) = 2.19 \times 10^{-5}$ eV^{-1} m$^{1/2}$ V$^{1/2}$ should be compared with the experimental values. It is clear that the predominant mechanism is SE in MS structures whereas PFE is dominant mechanism in MPS-type SDs at the reverse bias voltage.

4. Conclusion

In this work, PVP with/without dopants was used as an interfacial layer at M/S interface to manufacture a MPS-type SD. Five different SDs called as MS, MPS1, MPS2, MPS3, and MPS4 were fabricated onto same p-Si wafer to examine the impact polymer interlayer on the performance of MS-type SD. The crystalline size, surface morphology, and band gap energy of the ZnTiO$_3$ nanostructures were studied by the XRD pattern, FESEM image, and UV–Vis spectroscopy analysis, respectively. The I–V characteristics of these SDs were measured at ±3 V to obtain their electrical parameters by using TE, Norde, and Cheung methods. The value of I_0 and n for MS diode was reduced when an interfacial polymer layer was applied between the metal and semiconductor while the BH value was raised. The higher value of n was attributed to the barrier inhomogeneity and interfacial layer at the M/S interface, image-force lowering, N_{ss}, dielectric constant, depletion layer width, and GR. The RR value of MPS4 structure where Gr-ZnTiO$_3$ nanostructures were used for doping the PVP layer is higher than that of the other diodes at ±3 V. The observed major reduction of N_{ss} value among these diodes was related to the MPS3 structure which was nearly 46 times lower than the MS-type SD. The CM in these SDs was examined at the forward and reverse bias voltages. The experimental values of β_{PF} were compared with the theoretical ones. It was found that SE and PFE were the dominant mechanisms in MS- and MPS-type SDs, respectively.

Data availability statement

The data cannot be made publicly available upon publication because they are not available in a format that is sufficiently accessible or reusable by other researchers. The data that support the findings of this study are available upon reasonable request from the authors.

ORCID iDs

Ali Barkhordari https://orcid.org/0000-0002-5523-2859
Yashar Azizian-Kalandaragh https://orcid.org/0000-0001-6181-3767

References

[1] Sze S M and Ng K K 2006 LEDs and Lasers *Phys. Semiconduct. Devices* **3** 601–57

[2] Nicollian E H and Brews J R 1982 *MOS (Metal Oxide Semiconductor) Physics and Technology* (New York: Wiley) p 920

[3] Card H C and Rhoderick E H 1971 Studies of tunnel MOS diodes I. Interface effects in silicon Schottky diodes *J. Phys. D: Appl. Phys.* **4** 1589

[4] Altındal Ş, Barkhordari A, Azizian-Kalandaragh Y, Çevrimli B S and Mashayekhi H R 2022 Dielectric properties and negative-capacitance/dielectric in Au/n-Si structures with PVC and (PVC: sm$_2$O$_3$) interlayer *Mater. Sci. Semiconduct. Process.* **147** 106754

[5] Al-Dharob M H, Lapa H E, Kökce A, Özdemir A F, Aldemir D A and Altındal Ş 2018 The investigation of current-conduction mechanisms (CCMs) in Au/(0.07 Zn-PVA)/n-4H-SiC (MPS) Schottky diodes (SDs) by using

(IVT) measurements *Mater. Sci. Semiconduct. Process.* **85** 98–105

[6] Yerişkin S A, Balbaşı M and Orak İ 2017 The effects of (graphene doped-PVA) interlayer on the determinative electrical parameters of the Au/n-Si (MS) structures at room temperature *J. Mater. Sci., Mater. Electron.* **28** 14040–8

[7] Çiçek O, Altındal S and Azizian-Kalandaragh Y 2020 A highly sensitive temperature sensor based on Au/graphene-PVP/n-Si type Schottky diodes and the possible conduction mechanisms in the wide range temperatures *IEEE Sens. J.* **20** 14081–9

[8] Reddy V R and Prasad C V 2018 Surface chemical states, electrical and carrier transport properties of Au/ZrO$_2$/n-GaN MIS junction with a high-k ZrO$_2$ as an insulating layer *Mater. Sci. Eng.* B **231** 74–80

[9] Tung R T 2014 The physics and chemistry of the Schottky barrier height *Appl. Phys. Rev.* **1** 011304

[10] Al-Ahmadi N A 2020 Metal oxide semiconductor-based Schottky diodes: a review of recent advances *Mater. Res. Express* **7** 032001

[11] Barkhordari A, Altındal Ş, Pirgholi-Givi G, Mashayekhi H, Özçelik S and Azizian-Kalandaragh Y 2023 The influence of PVC and (PVC:SnS) interfacial polymer layers on the electric and dielectric properties of Au/n-Si structure *Silicon* **15** 855–65

[12] Baraz N, Yücedağ İ, Azizian-Kalandaragh Y and Altındal Ş 2017 Determining electrical and dielectric parameters of dependence as function of frequencies in Al/ZnS-PVA/p-Si (MPS) structures *J. Mater. Sci., Mater. Electron.* **28** 1315–21

[13] Sharma M and Tripathi S K 2016 Frequency and voltage dependence of admittance characteristics of Al/Al$_2$O$_3$/PVA:n-ZnSe Schottky barrier diodes *Mater. Sci. Semiconduct. Process.* **41** 155–61

[14] Erbilen Tanrıkulu E, Altındal Ş and Azizian-Kalandaragh Y 2018 Preparation of (CuS–PVA) interlayer and the investigation their structural, morphological and optical properties and frequency dependent electrical characteristics of Au/(CuS–PVA)/n-Si (MPS) structures *J. Mater. Sci., Mater. Electron.* **29** 11801–11

[15] Kumar N and Chand S 2020 Effects of temperature, bias and frequency on the dielectric properties and electrical conductivity of Ni/SiO$_2$/p-Si/Al MIS Schottky diodes *J. Alloys Compd.* **817** 153294

[16] Rajagopal Reddy V, Manjunath V, Janardhanam V, Leem C H and Choi C J 2015 Double Gaussian distribution of barrier heights, interface states, and current transport mechanisms in Au/Bi$_{0.5}$Na$_{0.5}$TiO$_3$-BaTiO$_3$/*n*-GaN MIS structure *J. Electron. Mater.* **44** 549–57

[17] Singh P, Kumar A and Kaur D 2008 ZnO nanocrystalline powder synthesized by ultrasonic mist-chemical vapour deposition *Opt. Mater.* **30** 1316–22

[18] Singh P, Kumar A and Kaur D 2008 Substrate effect on texture properties of nanocrystalline TiO$_2$ thin films *Physica* B **403** 3769–73

[19] Wang N, Li X, Wang Y, Hou Y, Zou X and Chen G 2008 Synthesis of ZnO/TiO$_2$ nanotube composite film by a two-step route *Mater. Lett.* **62** 3691–3

[20] Rao B B 2000 Zinc oxide ceramic semi-conductor gas sensor for ethanol vapour *Mater. Chem. Phys.* **64** 62–65

[21] Yoshino Y, Makino T, Katayama Y and Hata T 2000 Optimization of zinc oxide thin film for surface acoustic wave filters by radio frequency sputtering *Vacuum* **59** 538–45

[22] Jäger S, Szyszka B, Szczyrbowski J and Bräuer G 1998 Comparison of transparent conductive oxide thin films prepared by ac and dc reactive magnetron sputtering *Surf. Coat. Technol.* **98** 1304–14

[23] Birkmire R W and Eser E 1997 Polycrystalline thin film solar cells: present status and future potential *Annu. Rev. Mater. Sci.* **27** 625–53

[24] Look D C 2001 Recent advances in ZnO materials and devices *Mater. Sci. Eng.* B **80** 383–7

[25] Bodade A B, Bende A M and Chaudhari G N 2008 Synthesis and characterization of CdO-doped nanocrystalline ZnO: tiO$_2$-based H$_2$S gas sensor *Vacuum* **82** 588–93

[26] Zhang X, Zhang F and Chan K Y 2006 The synthesis of Pt-modified titanium dioxide thin films by microemulsion templating, their characterization and visible-light photocatalytic properties *Mater. Chem. Phys.* **97** 384–9

[27] Kim H T, Nahm S, Byun J D and Kim Y 1999 Low-fired (Zn,Mg) TiO$_3$ microwave dielectrics *J. Am. Ceram. Soc.* **82** 3476–80

[28] Obayashi H, Sakurai Y and Gejo T 1976 Perovskite-type oxides as ethanol sensors *J. Solid State Chem.* **17** 299–303

[29] Shimizu Y, Komatsu H, Michishita S, Miura N and Yamazo N 1996 Sensing characteristics of hydrogen peroxide sensor using carbon-based electrode loaded with perovskite-type oxide *Sens. Actuators* B **34** 493–8

[30] Wang S F, Lü M K, Gu F, Song C F, Xu D, Yuan D R, Zhou G J and Qi Y X 2003 Photoluminescence characteristics of Pb^{2+} ion in sol–gel derived ZnTiO$_3$ nanocrystals *Inorg. Chem. Commun.* **6** 185–8

[31] Gabrovska M, Edreva-Kardjieva R, Tenchev K, Tzvetkov P, Spojakina A and Petrov L 2011 Effect of Co-content on the structure and activity of Co–Al hydrotalcite-like materials as catalyst precursors for CO oxidation *Appl. Catal.* A **399** 242–51

[32] Gui Y, Li S, Xu J and Li C 2008 Study on TiO$_2$-doped ZnO thick film gas sensors enhanced by UV light at room temperature *Microelectron. J.* **39** 1120–5

[33] Wang S F, Gu F, Mk L, Song C F, Xu D, Yuan D R and Liu S W 2003 Photoluminescence of sol–gel derived ZnTiO$_3$:Ni^{2+} nanocrystals *Chem. Phys. Lett.* **373** 223–7

[34] Dulln F H and Rase D E 1960 Phase equilibria in the system ZnO-TiO$_2$ *J. Am. Ceram. Soc.* **43** 125–31

[35] Steinike U and Wallis B 1997 Formation and structure of Ti-Zn-oxides *Cryst. Res. Technol.* **32** 187–93

[36] Chang Y S, Chang Y H, Chen I G, Chen G J, Chai Y L, Fang T H and Wu S 2004 Synthesis, formation and characterization of ZnTiO$_3$ ceramics *Ceram. Int.* **30** 2183–9

[37] Hou L, Hou Y D, Zhu M K, Tang J, Liu J B, Wang H and Yan H 2005 Formation and transformation of ZnTiO$_3$ prepared by sol–gel process *Mater. Lett.* **59** 197–200

[38] Durmus Z, Durmus A and Kavas H 2015 Synthesis and characterization of structural and magnetic properties of graphene/hard ferrite nanocomposites as microwave-absorbing material *J. Mater. Sci.* **50** 1201–13

[39] Barkhordari A, Özçelik S, Pirgholi-Givi G, Mashayekhi H R, Altındal Ş and Azizian-Kalandaragh Y 2022 Dielectric properties of PVP:BaTiO$_3$ interlayer in the Al/PVP:BaTiO$_3$/P-Si structure *Silicon* **14** 5437–43

[40] Altındal Ş, Barkhordari A, Özçelik S, Pirgholi-Givi G, Mashayekhi H R and Azizian-Kalandaragh Y 2021 A comparison of electrical characteristics of Au/n-Si (MS) structures with PVC and (PVC:Sm$_2$O$_3$) polymer interlayer *Phys. Scr.* **96** 125838

[41] Barkhordari A, Özçelik S, Altındal Ş, Pirgholi-Givi G, Mashayekhi H and Azizian-Kalandaragh Y 2021 The effect of PVP:BaTiO$_3$ interlayer on the conduction mechanism and electrical properties at MPS structures *Phys. Scr.* **96** 085805

[42] Bilkan Ç 2020 Determination of structural properties of some important polymers used as interfacial layer in fabrication of schottky barrier diodes (SBDs) *J. Inst. Sci. Technol.* **10** 225–33

[43] Ashiri R, Nemati A, Ghamsari M S, Sanjabi S and Aalipour M 2011 A modified method for barium titanate nanoparticles synthesis *Mater. Res. Bull.* **46** 2291–5

[44] Ansaree J and Upadhyay S 2015 Thermal analysis of formation of nano-crystalline $BaTiO_3$ using Ba $(NO_3)_2$ and TiO_2 *Process. Appl. Ceram.* **9** 181–5

[45] Yu P, Cui B and Shi Q 2008 Preparation and characterization of $BaTiO_3$ powders and ceramics by sol–gel process using oleic acid as surfactant *Mater. Sci. Eng.* A **473** 34–41

[46] Altındal Ş, Barkhordari A, Pirgholi-Givi G, Ulusoy M, Mashayekhi H, Özçelik S and Azizian-Kalandaragh Y 2021 Comparison of the electrical and impedance properties of Au/(ZnOMn: PVP)/n-Si (MPS) type Schottky-diodes (SDs) before and after gamma-irradiation *Phys. Scr.* **96** 125881

[47] Fuentes S, Zárate R A, Chávez E, Muñoz P, Ayala M, Espinoza-González R and Leyton P 2010 Synthesis and characterization of $BaTiO_3$ nanoparticles in oxygen atmosphere *J. Alloys Compd.* **505** 568–72

[48] Gomez-Yañez C, Benitez C and Balmori-Ramirez H 2000 Mechanical activation of the synthesis reaction of $BaTiO_3$ from a mixture of $BaCO_3$ and TiO_2 powders *Ceram. Int.* **26** 271–7

[49] Parhoodeh S and Kowsari M 2016 Synthesis, characterization and study of band gap variations of vanadium doped indium oxide nanoparticles *Physica* B **498** 27–32